Surface & Coatings Technology 281 (2015) 184–192

Contents lists available at ScienceDirect

Surface & Coatings Technology

journal homepage: www.elsevier.com/locate/surfcoat

Structure and properties of Cr–C/Ag films deposited by magnetron sputtering

M. Folkenant [a], K. Nygren [a,b], P. Malinovskis [a], J. Palisaitis [c], P.O.Å. Persson [c], E. Lewin [a,*], U. Jansson [a]

[a] Department of Chemistry — Ångström Laboratory, Uppsala University, Box 538, 751 21 Uppsala, Sweden
[b] Impact Coatings AB, Westmansgatan 29, SE-58216, Linköping, Sweden
[c] Thin Film Physics Division, Department of Physics, Chemistry and Biology (IFM), Linköping University, SE-581 83 Linköping, Sweden

ARTICLE INFO

Article history:
Received 5 June 2015
Revised 18 September 2015
Accepted in revised form 28 September 2015
Available online 22 October 2015

Keywords:
Amorphous
Chromium carbide
Silver
Magnetron sputtering
Mechanical properties
Electrical properties

ABSTRACT

Cr–C/Ag thin films with 0–14 at.% Ag have been deposited by magnetron sputtering from elemental targets. The samples were analyzed by X-ray diffraction, transmission electron microscopy, X-ray photoelectron spectroscopy (XPS) and scanning electron microscopy (SEM) to study their structure and chemical bonding. A complex nanocomposite structure consisting of three phases; nanocrystalline Ag, amorphous CrC_x and amorphous carbon is reported. The carbon content in the amorphous carbide phase was determined to be 32–33 at.% C, independent of Ag content. Furthermore, SEM and XPS results showed higher amounts of Ag on the surface compared to the bulk. The hardness and Young's modulus were reduced from 12 to 8 GPa and from 270 to 170 GPa, respectively, with increasing Ag content. The contact resistance was found to decrease with Ag addition, with the most Ag rich sample approaching the values of an Ag reference sample. Initial tribological tests gave friction coefficients in the range of 0.3 to 0.5, with no clear trends. Annealing tests show that the material is stable after annealing at 500 °C for 1 h, but not after annealing at 800 °C for 1 h. In combination, these results suggest that sputtered Cr–C/Ag films could be potentially applicable for electric contact applications.

© 2015 The Authors. Published by Elsevier B.V. This is an open access article under the CC BY-NC-ND license (http://creativecommons.org/licenses/by-nc-nd/4.0/).

1. Introduction

Transition-metal carbide thin films are potential candidates for applications where high hardness, high wear resistance, low friction and high corrosion resistance are important properties. Transition metal carbides also have high electrical conductivity, which suggests a potential use as coatings in sliding electrical contacts as an alternative to e.g. Ag, which has been demonstrated for several materials systems [1–3]. One alternative contact material could be Cr–C films, due to the very high oxidation resistance of such films [4–6]. However, unpublished pin-on-disk measurements (by the authors) on Cr–C films have shown that the friction coefficient against ball-bearing steel at a normal load of 2 N and at room temperature is about 0.4, which is too high in many applications. The present study confirms these results and investigates a modification of Cr–C films, intended to reduce the friction coefficient, while maintaining a high corrosion resistance and low wear rate.

Several groups have studied the influence of Ag to Cr–N with the motive to lower the friction coefficient, see e.g. Ref. [7–10]. The results show that CrN–Ag films consist of a crystalline CrN matrix with embedded Ag nanocrystallites in the bulk and in many cases also Ag particles on the surface. Furthermore, the Ag particles within the bulk segregates easily during annealing at about 500–700 °C to form a higher amount of Ag on the surface. The Ag segregation has also proven to contribute to even lower friction coefficients for both annealed samples and for tribological tests conducted at elevated temperatures [11–14]. It is likely that the addition of Ag to Cr–C films could exhibit similar behavior with a reduced friction coefficient, with maintained high conductivity and thus with possible applications in electrical contacts.

The aim of this study is to investigate the effect of Ag addition to magnetron sputtered Cr–C films. In particular, we report on the structure and chemical bonding and how it influences mechanical, tribological and electrical properties. As this is a first study in the present materials system focus will be on material structure, bonding and morphology; properties will not be studied in detail, but enough to determine if further studies are warranted. The influences of Ag addition to carbides and nitrides on e.g. the mechanical and electrochemical properties have been studied in several other systems, such as VN/Ag [15], Mo_2N/Ag [16], TaN–Ag [17], NbN/Ag [18], Zr–C–N–Ag [19], CrAlN–Ag [20], TiC–Ag [21,22] and WC–Ag [22]. As the chemical interactions between Ag and C or N generally are very weak, and the interactions between the used transition metals and C or N are strong, it is expected that Ag forms a separate phase. This is also observed as these Me–X/Ag films (where X is either C or N) generally are nanocomposites consisting of Ag grains embedded in a nanocrystalline or nanocomposite Me–X matrix. For the Cr–C/Ag system however, we expect a more

* Corresponding author.
E-mail address: erik.lewin@kemi.uu.se (E. Lewin).

http://dx.doi.org/10.1016/j.surfcoat.2015.09.054
0257-8972/© 2015 The Authors. Published by Elsevier B.V. This is an open access article under the CC BY-NC-ND license (http://creativecommons.org/licenses/by-nc-nd/4.0/).

complex microstructure since non-reactive sputtering in the binary Cr–C system is known to produce amorphous nanocomposite coatings with an amorphous chromium carbide (a-CrC_x) phase and an amorphous carbon (a-C) matrix [4,23]. This is a very different microstructure than other carbide or nitride systems that have been the basis of the Me–X/Ag materials previously studied. Thus the addition of Ag to Cr–C may give interesting new possibilities, and may also be a way to modify the amorphous microstructure of the binary material and this will therefore be studied in detail.

2. Material and methods

Cr–C/Ag thin films were deposited using non-reactive DC magnetron sputter deposition in an ultra-high vacuum (UHV) chamber. The system has four magnetrons mounted in a confocal sputter-down configuration with a target to substrate distance of 14 cm and a sputtering angle of 24° relative to the substrate normal. Latterly homogeneous coatings are ensured by a substrate rotation of about 10 rpm. The base pressure in the deposition chamber was 10^{-7} Pa, for all depositions and Ar gas was let into the chamber during deposition at a pressure of 0.4 Pa. Co-sputtering was performed from 2-inch circular targets. Of the four magnetrons, two were equipped with C targets, one with a Cr target and one with a segmented target, assembled of three quarters of Cr and one quarter of Ag. All targets were obtained from Kurt J. Lesker Ltd. with claimed purities for the C, Cr and Ag targets of 99.999%, 99.95% and 99.99% respectively. In total, films with six different compositions were deposited by tuning the Cr (180 to 42 mA) and Cr/Ag (0 to 150 mA) magnetron currents while keeping the C magnetron currents constant at 300 mA, with the aim of keeping the total carbon content in the series constant. The deposition rate was about 5 nm/min for all films. The substrates used were Si (001) for X-ray photoelectron spectroscopy (XPS), X-ray diffraction (XRD) and scanning electron microscopy (SEM), while α-Al_2O_3 (001) was used for resistivity measurements, nanoindentation and for annealing and related analyses, such as SEM, and XPS depth profiles. Furthermore, mirror polished 316L stainless steel substrates were used for electrochemical, tribological and contact resistance measurements. Prior to deposition, the substrates were ultrasonically cleaned for 5 min each in isopropanol and ethanol and blow-dried using N_2 gas. No external heating was used during the process. To further clean the substrates, plasma etching was used for 5 min prior to deposition (−400 V bias, 25 mA Cr current) and a 25 nm thick Cr binding layer was deposited to improve adhesion and minimize reactions between Ag and the Si substrate. The Cr–C/Ag layers were deposited with a floating substrate potential for 180 min resulting in a thickness of 0.9–1.1 μm depending on the used target currents. Sample thickness was smallest for pure Cr–C film and a slightly increase was observed with increasing Ag content. However, one sample was unintentionally deposited for a longer time, resulting in a thickness of 1.6 μm.

Film composition, Ag bulk distribution and chemical bonding were analyzed by XPS using a PHI Quantum 2000 spectrometer with monochromatic Al Kα radiation. The binding energy scale was calibrated against reference samples using the Au4f, Ag3d and Cu2p peaks [24]. The film compositions were determined by depth profiling with sputtering of 1 keV Ar^+ ions rastered over a 1 × 1 mm area. Depth profile sputtering was carried out for 10 min in total, resulting in a maximum analysis depth of 45 nm using calibrated sputter rates. The compositions were then calculated by an average of bulk intensities below the oxidized surface region. Sensitivity factors were determined using elastic recoil detection analysis (ERDA) with 36 MeV $^{127}I^+$ on three Cr–C/Ag samples. Additionally, due to the overlap of the Ag and I peaks in ERDA, the Ag content has also been analyzed using RBS and resulted in a consistent Ag content with a maximum difference of ±1.5 at.%. Finally, the chemical bonding was analyzed by acquiring high-resolution spectra after pre-sputtering using 0.2 keV Ar^+ ions. The lower Ar^+ ion energy was used to avoid sputter damages and the analyses were carried out in the constant composition region below the oxidized surface used to determine the composition in the depth profiles. The film crystallinity was investigated by grazing incidence X-ray diffraction using a Philips MRD X'pert diffractometer with Cu Kα radiation and parallel beam geometry and an incidence angle of 1°. Lattice parameters were determined using all observed diffraction peaks and regression analysis as implemented in the software UnitCell [25]. A Zeiss Merlin SEM, equipped with energy-selective backscatter (EsB) and energy-dispersive X-ray spectroscopy (EDS) detectors, was used to analyze the film microstructure of fractured samples deposited on Si substrates as well as the Ag distribution in both cross-section and on surface (top-view). For the transmission electron microcopy (TEM) analysis, electron transparent cross-section samples were prepared from as-deposited structures by cutting the sample to small pieces, immobilizing them onto a Ti grid, gluing and mechanically polishing using diamond paper from both sides down to ~50 μm thickness. Further thickness reduction was achieved by Ar^+ ion milling in a Gatan precision ion polishing system (PIPS) while cooling the sample with liquid nitrogen. The first milling step was performed using 5 keV ion energy at a 5° angle with gradually reduced energy to 2 keV during the final step of milling to reduce the surface damage. The TEM analyses were performed in the Linköping double-corrected FEI Titan^3 60–300, operated at 300 kV. EDX mapping were acquired using the embedded high speed, high sensitivity Super-X detector.

To study film stability and Ag segregation, selected films on Al_2O_3 substrates were annealed in an UHV furnace with a pressure of about 1×10^{-5} Pa at either 500 °C or 800 °C. The temperature was ramped up for 30 min to the target temperature, held still for 60 min, and ramped down for 30 min. After the heating stopped, the temperature in the oven dropped rapidly at high temperatures, but took nearly 9 h to reach room temperature. The samples were analyzed both before and after annealing using XRD, XPS and SEM.

The mechanical properties were analyzed using a CSM Instruments Ultra Nano Hardness Tester (UNHT). All measurements were performed using a Berkovich diamond tip. For each sample, 20 indentations were made with a maximum indentation depth of 90 nm and the results were evaluated according to the Oliver–Pharr method [26]. The electrical resistivity was determined by first measuring the sheet resistance using a four-pin tungsten carbide probe (Jandel Engineering) connected to a highly sensitive voltmeter (Agilent Technologies 34420A), and then calculated by multiplying sheet resistance with respective film thickness. Electrical contact resistance was obtained from a four-wire setup, where an Au/Ni probe with a diameter of 1.4 mm was pressed against the sample surface while the voltage drop across the junction was measured. Further details are given elsewhere [27,28]. Three measurements were made per sample and average values are presented. The friction coefficient was measured using a custom built ball-on-disk setup with rotating geometry. The rotational radius was 3 mm and the sliding speed was 0.1 m/s. The counter surface was a ball bearing steel (AISI 52100, HRC60/66, $R_A < 0.5$ μm) ball with a diameter of 6 mm, and the film was subjected to a normal load of 2 N. The measurements were performed at about 30% relative humidity and 21 °C and a test duration of maximum 15,000 revolutions. A WYKO NT1100 optical profilometer was used for determining surface roughness, as well as coating wear after tribological testing; the latter calculated in accordance with the ASTM G 99-05 standard [29].

3. Results

Results from six samples are reported in this study, where the films have an Ag content ranging from 0 to 14 at.%. The compositional data is presented in Table 1, and as can be seen in the table, the carbon content is constant at 40 ± 1.5 at.% for all films, while the Cr content is reduced from 58 at.% to 47 at.% with increasing Ag content. XPS depth profiles show that the Ag-containing films exhibit a slightly thicker oxidized region at the surface than the Cr–C film. The film composition has been

Table 1
Summary over composition, and other microstructural parameters of the as-deposited samples.

Sample	Ag content (at.%)	Cr content (at.%)	C content (at.%)	Whereof a-C (at.%)	x in CrC_x	O content (at.%)
Cr–C	0	58	40	28	0.50	2
Cr–C/Ag2	2	55	42	33	0.51	2
Cr–C/Ag5	5	54	40	30	0.52	1
Cr–C/Ag9	9	50	40	36	0.52	1
Cr–C/Ag11	11	48	40	42	0.49	1
Cr–C/Ag14	14	47	38	41	0.48	1

calculated from XPS depth-profile intensities below the oxidized region, where the composition is constant. The oxygen content in the bulk is estimated to 1–2 at.% from the XPS depth profile results.

Preliminary depositions (not included in the results here) of Cr–C/Ag films deposited using the same equipment, and with a Ag content of about 50 at.% were made both at a substrate temperature of 300 °C and without intentional heating. Earlier studies on Cr–C films deposited in the same system used a substrate temperature of 300 °C [4]. However, the depositions at 300 °C resulted in a very porous structure for the Cr–C/Ag films, probably due to high Ag mobility during growth, which could cause segregation during film growth and in turn cause voids. However, the films deposited without intentional heating resulted in much denser films. Therefore, in order to obtain dense films, the films presented in this paper were deposited without intentional heating.

Fig. 1a shows the XRD diffractograms of the as-deposited films. There are no visible peaks in the diffractograms for the pure Cr–C film, only two broad features located at 40.5° and 79°. These features originate from the short-range order in the material and are located at approximately the same angles (40° and 80°) compared to the previously reported Cr–C films [4]. Thus it can be concluded this film is X-ray amorphous. The Cr adhesion layer is not visible in these GIXRD measurements, probably due to limited depth sensitivity at the chosen incident angle in combination with a very thin adhesion layer. In addition to these broad features related to amorphous Cr–C, five broad peaks become visible with increasing Ag content. These can all be indexed to cubic Ag with a cell parameter of 4.09 Å, which matches the reported bulk value [30]. For the samples Cr–C/Ag5, Cr–C/Ag9 and Cr–C/Ag14, the Ag grain size was estimated to 2–3 nm using Scherrer's equation for the Ag(111) peak located at 38.2°. The crystallinity of the Cr–C/Ag films was studied using high-resolution TEM (HRTEM) imaging and selective area electron diffraction (SAED). Typical HRTEM and SAED images for the Cr–C, Cr–C/Ag5 and Cr–C/Ag14 samples are shown in Fig. 2. The Cr–C sample has amorphous structure, where only very few subordered domains are seen. However, most of the images show no crystallinity, which is in agreement with the XRD results. Additionally, TEM high angle annular dark field (STEM-HAADF) at strong mass-contrast imaging conditions was set employed to investigate the samples. Images obtained from the Cr–C sample reveal a columnar structure exhibiting bright domains of higher mass, and embedding domains with darker contrast, and thus indicating a lower mass. The differences in contrast indicate two compositionally different phases in the Ag-free sample. Complimentary STEM–EDX analysis, see Fig. 3, show that the bright areas are Cr-rich while the dark areas represent a Cr-deficient phase, thus further support the existence of two phases in the film.

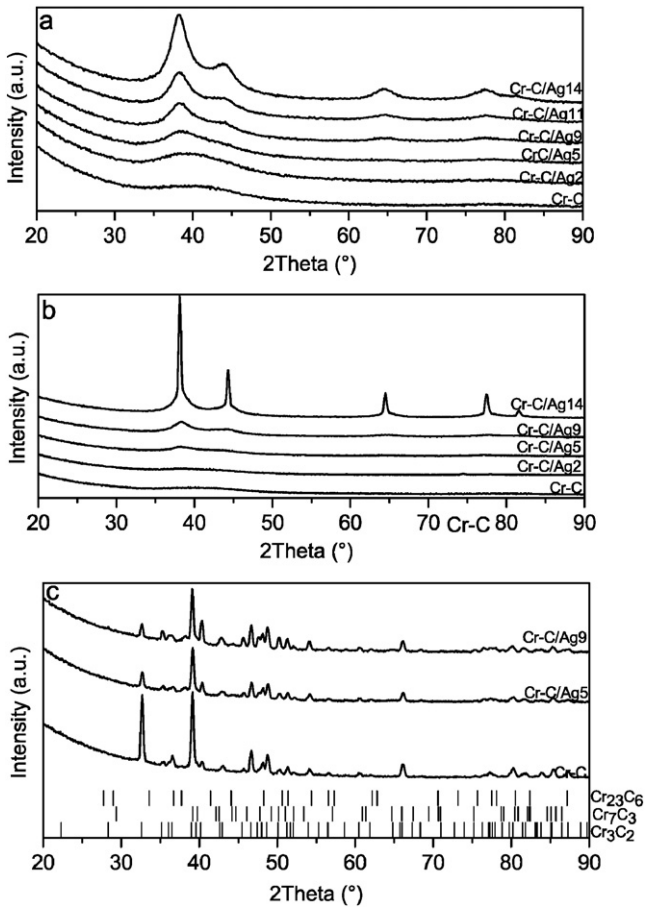

Fig. 1. X-ray diffractograms for a) as-deposited samples, b) after 60 min annealing at 500 °C and c) after 60 min annealing at 800 °C.

For the Ag-containing Cr–C/Ag5 and Cr–C/Ag14 samples, a crystalline phase is observed and clearly resolved by HRTEM and SAED. The typical crystallites size is ~2–5 nm, but larger grains of about 10–20 nm are also seen for Cr–C/Ag14. The identity of the crystalline phases observed by HRTEM was further investigated by STEM-HAADF imaging and STEM–EDX analysis. These crystallites are observed as bright particles in the STEM-HAADF images of the Ag containing samples, see Fig. 3. The STEM–EDX map reveal that in addition to the Cr-rich and Cr-deficient phases, the crystalline phases consist of Ag.

Both the surface of the film (top-view) and the microstructure of the bulk (cross-sections of fractured samples) have been analyzed using SEM, see Fig. 4. The cross-section SEM analysis of the Cr–C film (Fig. 4a) shows a columnar microstructure with an approximate column width of 30 nm. The cross-section SEM images of the Cr–C/Ag5 and Cr–C/Ag14 films are shown in Fig. 4b and c, respectively. For the Cr–C/Ag14 film, hints of very small, bright particles, smaller than 10 nm, dispersed in the bulk are also visible in the cross-section. Fig. 4d–f show SEM images of the surface of the as-deposited Cr–C, Cr–C/Ag5 and Cr–C/Ag14 films. The Ag-free Cr–C film exhibits a nodular-shaped surface with an even appearance. This nodular structure is also visible for the Ag-containing films, but additional ~20 nm large particles (with a brighter contrast than the underlying film) are visible on the surface. It should be noted that smaller particles might also be present on the surface even though they are not seen in the SEM image.

The SEM analysis also shows quite large numbers of dome-shaped features on the surface of about 200–500 nm in diameter. They are also visible in cross-section SEM (see inset in Fig. 4), where it is seen that they are cone-shaped. Results from EDX and SEM using EsB detector (not shown) shows no difference in composition compared to the surrounding material, suggesting that the cone-shaped features consist of Cr–C with about the same. Since these features are present for both Ag-containing films and the Cr–C film, and there is no trend in their amount related to the Ag content, the cone-shaped features seem to originate from deposition-related issues rather than from a side-effect of the Ag addition.

The XRD, TEM–EDX and SEM results together, suggest that the films consist of Ag nanocrystallites in an amorphous two-phase matrix. Furthermore, the SEM results show that the surface exhibits a rather high amount of Ag particles on the surfaces while fewer particles are seen

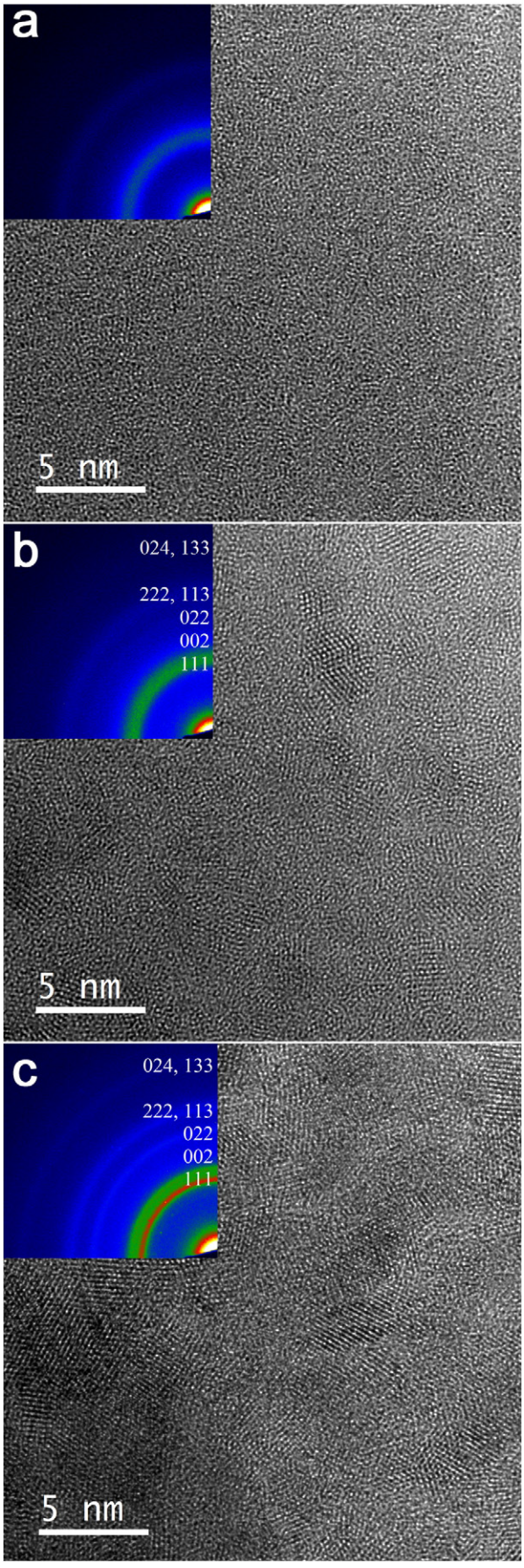

Fig. 2. Cross section HRTEM images of as-deposited films as well as SAED insets for Cr–C, Cr–C/Ag5 and Cr–C/Ag14 films. Indices for fcc-Ag shown in SAED-insets.

in the cross-sections, which jointly indicates a higher content of Ag on the surface than in the bulk. To analyze this further, XPS depth profiles were studied and the ratio of the Ag 3d intensity on surface and in bulk (after Ar^+ ion etching) was plotted against the Ag content. The result is seen in Fig. 5 and it shows a clear enrichment of Ag on the surface compared to the bulk concentration as the intensity ratio is above 1. This is more pronounced for low Ag contents. A possible explanation for this could be the more columnar structure of the Ag-poor samples that could facilitate a larger mobility of the Ag atoms during sample growth, and thus a larger degree of surface segregation. Furthermore, chemical bonding has been studied by peak fittings of high-resolution XPS spectra, as shown in Fig. 6. For the C1s XPS peak only three contributions are needed to fit the data, C–Cr, C–C and C–O; where the C–Cr peak is located at a binding energy of 282.8 eV, the C–C peak at 284.3 eV and the very small C–O peak at 286.1 eV. The positions of the C–Cr and C–C peaks are consistent with previous work on amorphous Cr–C thin films [4]. Peak fittings of the Cr2p peaks were also performed (not shown). The only change in the Cr2p spectra is attributed to the overlap from the Ag3p 3/2, positioned at 573.0 eV, and thus very close to the Cr2p 3/2 peak at 574.2 eV. This small Ag3p-contribution in the Cr2p region will of course influence the intensity used in the depth profiles for compositional analysis, however the contribution is so small that the influence on the calculated composition is less than 1 at.% and may thus be ignored within the present precision. The Ag3d 5/2 peak (not shown) is located at 368.2 eV, which is in exact agreement with the Ag reference used for calibration and no shift is seen with increasing Ag content.

The C1s XPS spectra clearly show the existence of two phases; one chromium carbide phase and one carbon phase. The XRD and TEM analyses show that the two phases are amorphous and they will from here on be denoted a-CrC_x and a-C. From peak fitting, it is seen that 27–40% of the carbon atoms are bonded in a-C and that more carbon is bonded in a-C at higher Ag contents (see inset in Fig. 6). Furthermore, from the total carbon and chromium contents together with the area intensities of C–Cr and C–C in the XPS C1s spectra, the carbon content in the a-CrC_x phase could be determined to vary between a-$CrC_{0.48}$ to a-$CrC_{0.52}$ (see Table 1). This correspond to an almost constant carbon content of 32–34 at.% for this phase in all films. This is based on the assumption that all Cr atoms are bonded to the a-CrC_x phase.

Annealing experiments were performed in an UHV tube furnace at 500 °C and at 800 °C for selected samples. The annealed films were analyzed using XRD, SEM and XPS to investigate the changes in both structure and bonding. GI-XRD results of the annealed samples at 500 °C, see Fig. 1b, show that there are no indications of crystalline Cr–C in any of the films and the only visible peaks originate from the Ag nanocrystallites. For sample Cr–C/Ag5 and Cr–C/Ag9, the slightly narrower peaks suggest a possible increase in grain size compared with the as-deposited case. However, for sample Cr–C/Ag14, the peaks are much narrower compared to both the as-deposited case and to the other annealed samples. The observed peaks are strong in intensity and have a quite broad base, suggesting Ag contributions of several sizes. For this sample, an estimated grain size of 30 nm was calculated from the four strongest peaks using the Scherrer equation. Also, the cell parameter was determined to be 4.09 Å, which is consistent with the cell parameter before annealing and for the cubic Ag bulk reference. The films annealed at 500 °C were also analyzed using SEM and images for sample Cr–C, Cr–C/Ag5 and Cr–C/Ag14 are illustrated in Fig. 4g–i. For the Cr–C film, no change is seen in the SEM images before and after annealing at 500 °C. For Cr–C/Ag5, small Ag particles about 40 nm in size are visible on the surface of the annealed sample and additional, larger Ag particles, of about 100–200 nm in size, are visible adjacent to the defects. Fig. 4i shows Cr–C/Ag14 where large Ag particles about 50–200 nm in size are seen on the surface. The other samples in the series (not shown) follow the same trend, where there is an increase in Ag particles near the defects for low Ag contents, while there are a larger amount of Ag particles also spread on the surface for higher Ag contents. The Cr–C/Ag14 sample, however, stands out, as in addition to these

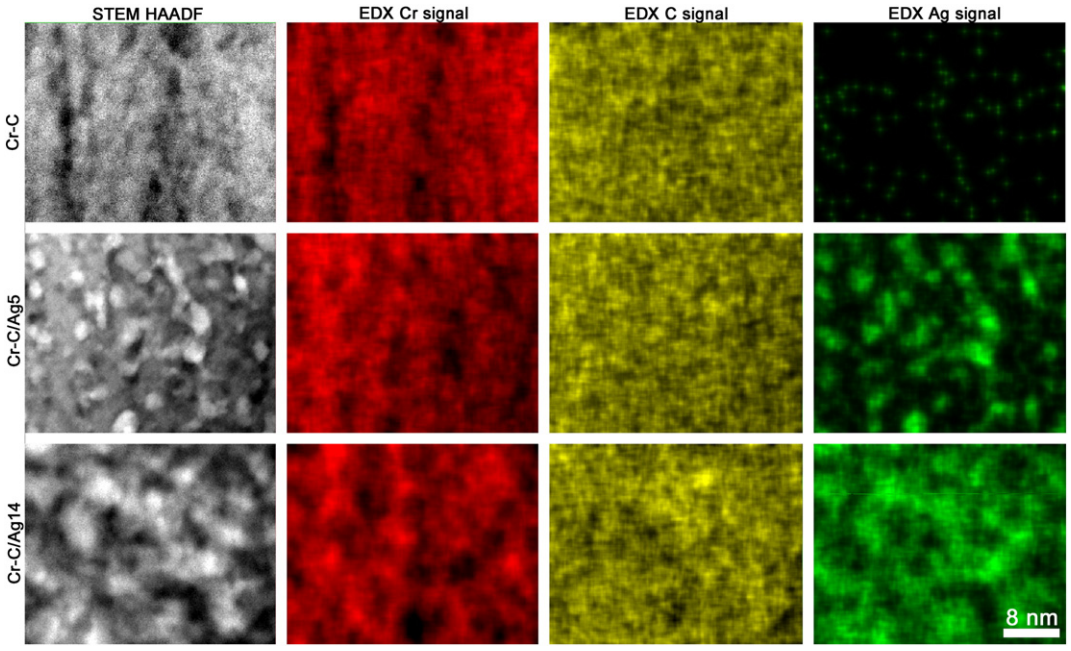

Fig. 3. STEM analysis of as-deposited samples, micrographs attained with HAADF detector in first column, and elemental signal from EDX mapping of the same areas in columns two through four. Binary Cr–C sample in the first row, low Ag-content sample Cr–C/Ag5 in the middle row and high Ag content sample Cr–C/Ag14 in the bottom row. Scale bar bottom right is valid for all images.

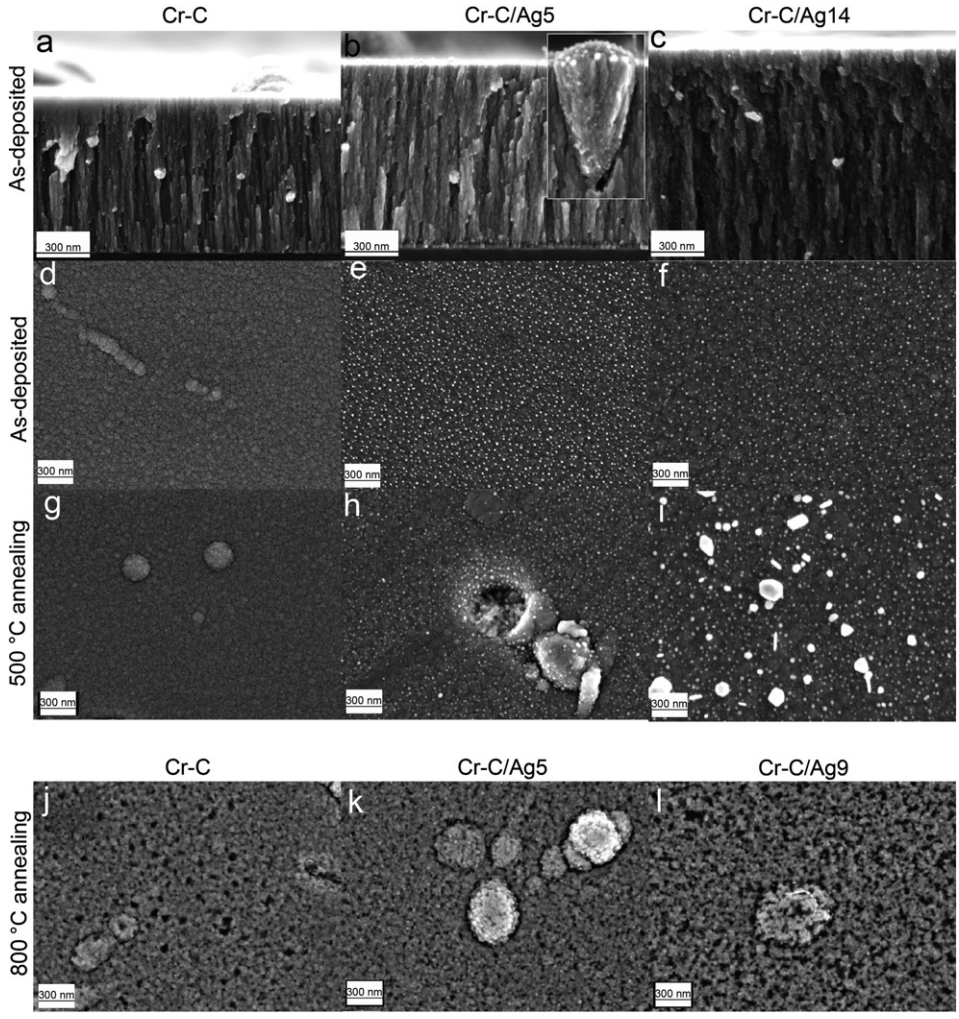

Fig. 4. SEM images of as-deposited samples in cross-section (first row) and top-view (second row) and after annealing at 500 °C (third row) for Cr–C (first column), Cr–C/Ag5 (second column) and Cr–C/Ag14 (third column) and after annealing at 800 °C (fourth row) for Cr–C (first column), Cr–C/Ag5 (second column) and Cr–C/Ag9 (third column). All scale bars are 300 nm wide.

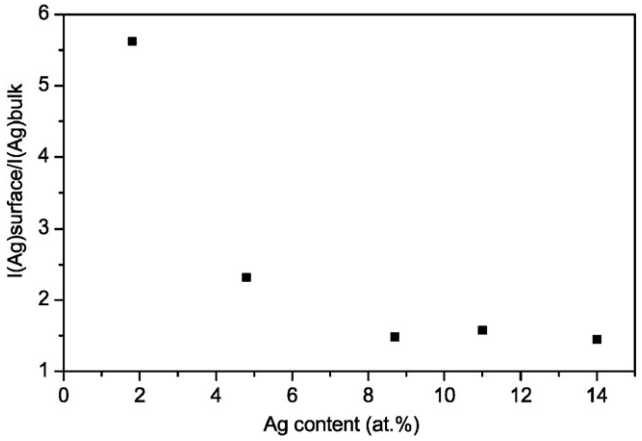

Fig. 5. The ratio of XPS Ag3d intensity data from surface and bulk plotted versus the bulk Ag content.

particles on the surface, it also exhibits many other kinds of outgrowths formed after the annealing at 500 °C. Fig. 7a (top panel) shows a tilted view of the surface where faceted outgrowths, extending from the film surface are visible. These outgrowths are up to μm-size in width, several μm in length, and often originated from, or at least near, the defects. Also, several tenths of μm long whiskers are seen, extending from the surface in different angles. Furthermore, very large particles of about 1–3 μm in diameter are also seen on the surface, especially around the defects. Fig. 7 shows additional analysis of the outgrowths, the bottom panel shows a SEM image of a whisker, analyzed with two different detectors, backscatter (ESB) detector (left) and secondary electron (SE) detector (right). In the ESB image the whisker appears brighter due to elemental contrast (heavier elements yield more contrast), which is a clear sign that the whisker consists of more Ag than the surrounding film surface. Fig. 7b shows EDS mapping of a large surface particle, which shows a clear increase of Ag, compared to the surrounding film surface. A dark area can also be noted beneath the particle and this effect is seen for all elements and is due to shadowing.

The changes in composition after annealing at 500 °C were analyzed using XPS. No significant changes in bulk composition were observed for Cr–C, Cr–C/Ag5 and Cr–C/Ag9. The carbon content in the a-CrC_x phase was estimated to 29–32 at.%, which is close to the content for the as-deposited films. However, in the Cr–C/Ag14 sample, analysis at a depth of 45 nm showed an increased in Ag content from 14 to 23 at.%, suggesting that the segregation of Ag towards the surface had started. There were no clear changes in Ag, Cr or O peak positions,

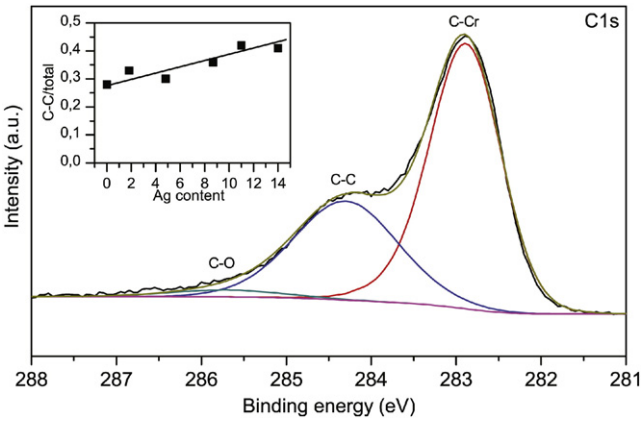

Fig. 6. Representative peak-fitted XPS C1s spectra with the C–Cr, C–C and C–O peaks located at 282.8 eV, 284.3 eV and 286.1 eV, respectively. Inset: Relative amount of C–C bonds (to total carbon bonds) versus the Ag content.

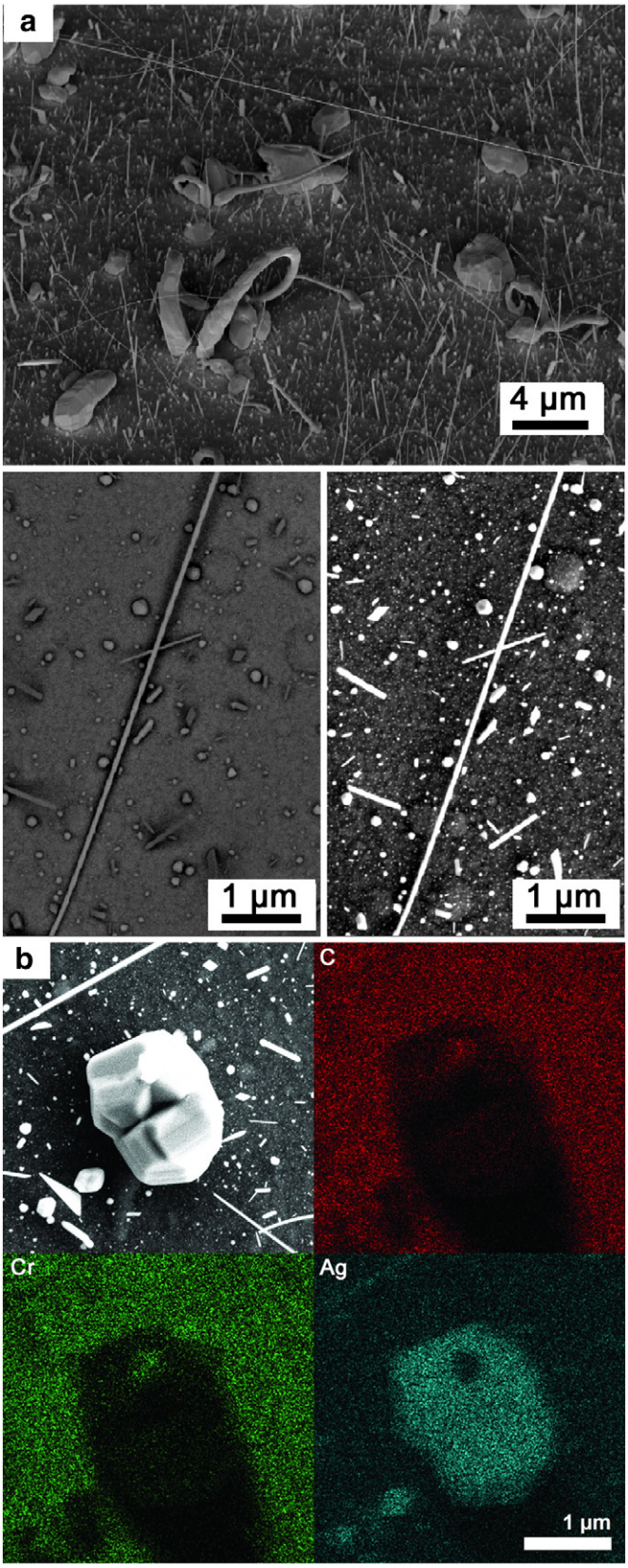

Fig. 7. a) Top panel: SEM image of tilted Cr–C/Ag14 sample after annealing at 500 °C. Bottom panel, EsB (left) and SE (right) detector images of whisker and other outgrowths on the Cr–C/Ag14 sample after annealing at 500 °C. b) SEM–EDS images of surface particle on Cr–C/Ag14 sample after annealing at 500 °C.

which otherwise could have suggested formation of silver chromate or silver oxide phase. However, the Cr–C/Ag14 sample showed much higher Ag surface intensity after annealing, consistent with the SEM analysis, indicating that the outgrowths on the surface of the Cr–C/Ag14 sample consist of Ag or at least an Ag-rich compound.

In addition, three separate samples of Cr–C, Cr–C/Ag5 and Cr–C/Ag14 (previously not annealed) were annealed at 800 °C. For these films, a large number of peaks emerge in the diffractograms after annealing. These peaks are consistent with the Cr_3C_2 carbide, even though contributions from the Cr_7C_3 carbide cannot be excluded due to some overlaps. The cell parameters of the orthorhombic Cr_3C_2 phase were determined to be a = 5.51 Å, b = 11.45 Å and c = 2.83 Å. Compared to the cell parameters of the bulk reference where a = 5.53 Å, b = 11.49 Å and c = 2.83 Å [31], the results show that the cell volume is somewhat smaller than literature data, which may indicate a non-stoichiometric composition with carbon vacancies in the present samples although a volume change due to stresses cannot be excluded. Moreover, no sharp Ag peaks are visible after annealing at 800 °C. XPS depth profiles of the films annealed at 800 °C confirm that the Ag content in the film is much lower after annealing than for the as-deposited films and that a gradient is formed, with no indications of Ag near the surface and a low Ag content deeper into the bulk. SEM analysis of the films annealed at 800 °C shows a porous morphology, which gets even more porous for the Ag-containing films, as seen in Fig. 4j–l. Also, no Ag particles are visible on the surface, only empty rings, with about the same sizes as for the surface particles seen the samples annealed at 500 °C. As will be discussed below, this shows that Ag has evaporated from the film surface.

Finally, the mechanical, electrical and tribological properties in the Cr–C/Ag films were studied for the as-deposited films. The mechanical properties were measured by nanoindentation and both hardness and Young's modulus are tabulated in Table 2. The hardness of the Cr–C sample, without added Ag, was measured to be 11.6 ± 0.5 GPa. The hardness then decreases with increasing Ag/Cr ratio to 7.8 ± 1.0 GPa. The Young's modulus also decreased with increasing Ag/Cr ratio from 267 ± 23 GPa down to 167 ± 15 GPa.

The electrical properties were characterized by measuring resistivity and contact resistance for as-deposited films and the results are also summarized in Table 2. The resistivity for the Cr–C sample, without any Ag, was 198 μΩ cm. Addition of Ag decreases the resistivity to 172 μΩ cm for the Cr–C/Ag14 sample. The electrical contact resistance depends on contact force, however, to facilitate comparison and describe the general trend as a function of Ag content, only values obtained at a force of 1.0 N are given. Without any addition of Ag, the contact resistance was 56 mΩ. Successively lower, and thus better, contact resistance values down to 23 mΩ were observed with increasing Ag content. A reference sample consisting of 1 μm Ag on stainless steel exhibited a value of 10 mΩ.

Tribological testing was conducted on coatings deposited on steel substrates, where the coating surface roughness (R_a) was found to be between 8 and 11 nm for as-deposited coatings, and between 9 and 15 nm for annealed samples. The friction coefficient was measured using a pin-on-disk setup against a ball bearing steel ball at room temperature. Overall, the friction coefficient increased from about 0.3 to about 0.4–0.5 for all as-deposited films up to about 15,000 revolutions. No clear trend with respect to Ag-content could be observed. The room temperature friction coefficient was also measured for samples CrC/Ag5 and CrC/Ag9 after annealing at 500 °C. Also here, no significant changes in friction coefficient were observed. The wear rate was determined for the CrC and CrC/Ag5 samples (both as-deposited and annealed) by examining wear tracks after 2 000 revolutions. The wear rate was found to vary between $0.3 * 10^{-4}$ and $1.0 * 10^{-4}$ mm^3/m, with no clear trends. The observed rate is about one order of magnitude higher than results reported for low wear nc-TiC/a-C nanocomposites [32].

Table 2
Summary over electrical and mechanical properties of the as-deposited samples.

Sample	Resistivity (μΩ cm)	Contact resistance (mΩ)	Hardness (GPa)	Young's modulus (GPa)
Cr–C	198 ± 11	56 ± 14	11.6 ± 0.5	267 ± 23
Cr–C/Ag2	217 ± 12	45 ± 4	11.4 ± 0.9	247 ± 16
Cr–C/Ag5	215 ± 12	39 ± 4	10.4 ± 0.8	220 ± 14
Cr–C/Ag9	185 ± 10	23 ± 1	9.6 ± 0.6	202 ± 9
Cr–C/Ag11	177 ± 9	n/a	8.0 ± 0.5	203 ± 8
Cr–C/Ag14	172 ± 9	n/a	7.8 ± 1.0	167 ± 15

4. Discussion

The XRD and HR-TEM analysis confirms that the Cr–C sample without Ag is predominantly amorphous with minor inclusions of subordered domains. These domains are about 1 nm in size and may be an indication that some nanocrystallites have started to form. However, it should be noted that electron beam exposures during TEM analysis can induce crystallization in amorphous carbide films and they may be artifacts [33,34]. Furthermore, the STEM-HAADF, STEM–EDX and XPS analysis support earlier findings that Cr–C can form an amorphous nanocomposite consisting of the two amorphous phases a-CrC_x and a-C [4,23]. However, it should be noted that it cannot be excluded that small amounts of Cr are also present in the a-C phase. A discussed in Ref. [4], amorphous Cr–C films are often seen in non-reactive sputtering processes, while crystalline films are more frequently obtained in reactive sputtering processes or with a high enough ion bombardment.

From the XRD and STEM results together with STEM–EDX, it can also be concluded that the Ag-containing Cr–C/Ag films consist of Ag nanocrystallites in an amorphous matrix. For a low Ag content, no clear Ag peaks are visible in the X-ray diffractogram and this can have two causes: either the nanocrystallites are too small or too few to be detected by XRD, or the Ag-rich areas are not crystallized enough at low Ag contents to be detected by XRD. However, the HRTEM and STEM-HAADF results show Ag nanocrystallites of about 2–5 nm also for the Cr–C/Ag5 sample, which confirms that Ag forms crystallites also at low concentrations. Crystallite size estimations using broadening in XRD has several issues. The method samples more or less the entire film, which means that an average of all particles, bulk and surface, is given. In this study, SEM clearly shows different size distributions in the bulk and surface, thus explaining the apparent mismatch between the crystallite radii from SEM and XRD.

Consequently, it can be concluded that the Cr–C/Ag films can be described as a three-phase material with Ag nanoparticles distributed in the bulk and on the surface of an a-CrC_x/a-C nanocomposite. This is not unexpected since the solubility of C and Cr in Ag and vice versa is very small. The solubility of Ag in chromium carbides has not been determined but it is likely that very small amounts of Ag can dissolve in the a-CrC_x phase during sputtering but the sensitivity of the EDX analysis is too low to confirm this. Furthermore, the XPS and SEM results also clearly show that Ag segregates to the surface (Fig. 5) and that larger Ag particles are formed on the surface than in bulk. This is in agreement with many other studies on Ag addition of magnetron sputtered nitride or carbide films [7,9,35].

A detailed analysis of the C1s peak shows that the carbon content in the a-CrC_x phase is in a very narrow range, 29–33 at.% C, including both as-deposited films and the films annealed at 500 °C. This is about the same content as in the crystalline Cr_7C_3 phase (30 at.% C) but less than in the Cr_3C_2 phase (40 at.% C). It is interesting to note that the total carbon content in the films is constant at about 40 at.% in all the films. This means that as the Ag content is increased, the Cr content is reduced in the film. Although the Cr content is changed, the composition of the a-CrC_x phase is constant. This explains the increased amount of a-C phase with increased Ag/Cr ratio, shown in the inset of Fig. 6. The very narrow range for the carbon content in the a-CrC_x phase also suggests

that a composition close to Cr_7C_3 is particularly stable in the amorphous state. This composition can also be compared with similar results from previous studies, where the carbon content in the a-CrC_x phase was calculated to be 23–30 at.% in [4] and 35 ± 2 at.% in [6]. The films studied in refs. [4,6] were deposited at other substrate temperatures and also with much broader range in total carbon content. It is possible that these parameters affect the most stable composition of the a-CrC_x phase. It should be noted, however, that the estimated composition of the a-CrC_x phase is based on the assumption that no Cr is dissolved in the a-C phase. From the EDX analysis, this possibility cannot be excluded.

The thermal stability of the amorphous Cr–C film is high. After annealing to 500 °C during 1 h, no indications of crystallization of the a-CrC_x phase is observed. After 1 h of annealing at 800 °C however, the XRD data show almost only peaks originating from the Cr_3C_2 phase. The formation of the Cr_3C_2 carbide suggests higher carbon content in the crystalline phase than in the amorphous counterpart, although the XPS results do not show any significant changes in the a-CrC_x carbon content after annealing. This suggest that a carbon-deficient Cr_3C_2 carbide has formed, which also is supported by the observed cell parameter data showing a smaller unit cell as expected for a carbon-deficient carbide phase. The formation of the Cr_3C_2 phase can be understood when comparing the different crystalline structures of chromium carbides, where the cell volumes of Cr_3C_2, Cr_7C_3 and $Cr_{23}C_6$ are 0.180 nm^3, 0.386 nm^3 and 1.211 nm^3 respectively. From a structural point of view, the Cr_3C_2 phase has the smallest unit cell and thus the simplest structure of the three carbides. Hence, even though the composition in the a-CrC_x phase is closer to the Cr_7C_3 carbide, a carbon-deficient carbide with Cr_3C_2 structure can be formed due to the simpler structure. The preferred crystallization of a less complex structure is frequently observed in amorphous films. For example, although no cubic CrC phase with NaCl structure is thermodynamically stable, formation of a metastable cubic CrC_{1-x} phase in sputtered [36], and ion-plated coatings [37]. Also Abdulkadhim et al. have observed that amorphous Cr_2AlC films during annealing initially form an hexagonal and metastable $(Cr,Al)_2C_x$ phase prior to the formation of the thermodynamically stable Cr_2AlC MAX-phase with a more complex crystal structure [38]. Since our films were annealed for only 60 min, it can be suspected that the final crystal structure has not yet been formed and that further structural changes could occur for longer annealing times.

The annealing also affected the Ag distribution in the films. At 500 °C, no Ag segregation or redistribution was observed for the films with lower Ag content. For the most Ag-rich film Cr–C/Ag14, however, a special surface morphology with large Ag-rich outgrowths and whiskers were formed. After annealing to 800 °C, the SEM analysis showed a porous surface morphology without any visible Ag particles and a Ag gradient in the bulk indicating a substantial loss of Ag during the annealing process. A direct comparison to CrN–Ag films is difficult, the microstructure of the here studied samples is clearly different, and so is the Ag-content — two factors that are known to influence the Ag segregation behavior [7,14].

To explain the behavior of Ag during annealing, especially at 800 °C, a description of the physics of metal nanoparticles is required. An increased migration rate of Ag towards the surface at higher temperatures is certainly an important factor contributing to the observed microstructure. In addition, however, other factors related to the physics of nanoparticles are likely to be important. It is well known that the melting point of a substance as well as the vapor pressure depend on the grain size. Different diffusion behavior depending on Ag grain size has, e.g., been observed for CrN/Ag nanocomposites: smaller particles have upon annealing been found to disappear in the bulk leaving voids, whilst larger particles have remained in the coating [7,14]. Castro et al. have investigated the melting point of Ag nanoparticles and observed that a 2–3 nm Ag particle melts at about 430 °C, which is more than 500 °C lower than the melting point of bulk Ag (960 °C) [39]. Consequently, the smallest Ag nanoparticles in the bulk and on the surface of our sputter-deposited films should have melted at an annealing temperature of 500 °C, although it is possible that the 20 nm nanoparticles on the surface did not melt at that annealing temperature. Furthermore, thermodynamics predict that the vapor pressure above a curved surface is higher than that of a flat surface [40], which should favor a more rapid evaporation of nano-sized Ag particles (solid or melted). These factors can explain the lack of visible Ag particles on the surface and the formation of an even more porous microstructure for the Ag-containing films. Also, the rather high vapor pressure and reduced melting point for small Ag particles can also be explain the Ag outgrowths and whisker formation of the most Ag-rich film at an annealing temperature of 500 °C. At this temperature, an Ostwald-like ripening effect is expected where small particles evaporate, which together with an increased surface diffusion rate leads to a coalescence of the smaller grains forming larger Ag outgrowths. Also the formation of the Ag-rich whiskers, observed in Fig. 7, can be explained by a vapor–liquid–solid (VLS)-like mechanism where the melted Ag nanoparticles interact with evaporated atoms. Further studies of the exact composition of the whiskers are required, however, to clarify the details in the growth mechanism.

Table 2 shows that addition of Ag reduces the hardness of the films. This can be due to two factors; i) with increasing Ag content, the Cr content goes down. Therefore less Cr is available to form a carbidic phase, and with the constant carbon content there will now be an excess of carbon. This excess results in formation of an additional a-C phase, which is soft, thereby reducing hardness ii) with increasing Ag/Cr ratio, soft Ag crystallites are added to the system, which could reduce the total hardness of the film. The $C–C/C_{tot}$ ratio for the Cr–C/Ag films changes from 0.28 to 0.42 with increasing Ag/Cr ratio. For the earlier deposited Cr–C films [4], the hardness decreased with 0.6 GPa for a change in $C–C/C_{tot}$ ratio of 0.11 to 0.41. Thus, the rather large change in hardness for the Cr–C/Ag films cannot only depend on the change in $C–C/C_{tot}$ ratio and must hence also depend on addition of Ag nanocrystallites.

One aims with this study was to explore the influence of Ag on the tribological properties. In room-temperature friction test no certain trends could be observed: after a while all samples exhibited about the same friction coefficient versus a steel surface as the Ag-free Cr–C film. It is well known that the addition of Ag improves the friction properties of many materials at elevated temperatures and an additional study of the tribological behavior of the Cr–C/Ag films at a higher temperature would be interesting, but is beyond the present study.

Overall, addition of Ag to Cr–C clearly reduced both resistivity and contact resistance. It should however be made clear that the effect on resistivity is not that great, and the values are in fact rather close to the ones obtained for Cr–C films reported previously [4]. On the other hand, the conductive Ag surface agglomerates clearly reduced the contact resistance, with the lowest value only being twice that of the Ag reference, even at the relatively low contact force. Furthermore, reactively sputtered Cr–C/a-C:H films exhibited a contact resistance about five times that of Ag [27], showing that the present Cr–C/Ag films have better contact properties. To confirm the functionality of the material, a separate study of contact resistance as a function of force and surface chemistry would be needed to further characterize the electrical contact properties for this material system. Furthermore, earlier research in the Cr–C system has shown that Cr–C thin films have beneficial electrochemical properties. However, adding a noble Ag phase into a mixture of a-CrCx, a-C, and possibly also metallic Cr, is a cause for concern regarding the corrosion resistance. The addition of a capping layer, however, could strongly improve these properties.

5. Conclusions

Nanocomposite Cr–C/Ag thin films, with up to 14 at.% Ag, have been deposited by non-reactive magnetron sputtering and the films have been found to consist of a complex three-phase structure, with Ag nanocrystallites embedded in an amorphous two-phase system of a-CrC_x and a-C. The a-CrC_x phase had a carbon content of 29–33 at.%,

independent of C/Cr ratio, which is consistent with earlier research within the Cr–C system. The as-deposited films contained Ag nanocrystallites of 2–5 nm in bulk and larger particles, up to 20 nm, were observed on the surface. The Ag content on the surface was also higher compared to that in the bulk. The amorphous phase was stable up to at least 500 °C, and after annealing a slight increase in the surface Ag content was observed for films with low Ag contents (≤9%). However, for the most Ag-rich film, with 14 at.% Ag, faceted outgrowths and whiskers were observed on the surface. Annealing at 800 °C in vacuum caused Ag to evaporate into gas-phase and additionally, the formation of a substoichiometric Cr_3C_2 phase was formed. The hardness reduces slightly due to the addition of soft Ag nanocrystallites. Room temperature pin-on-disk measurements on as-deposited and annealed samples showed no major change in friction coefficient as a result Ag addition or annealing up to 500 °C. The electrical properties improved by addition of Ag, where the contact resistance decreased and approached values only twice that of an Ag reference film.

Acknowledgments

Daniel Primetzhofer from Ion-Physics group at Uppsala University is acknowledged for the ERDA measurements. The authors also acknowledge the Knut and Alice Wallenberg Foundation for support of the Electron Microscopy Laboratory in Linköping. The Swedish Foundation for Strategic Research, SSF (FunCase, RMA11-0029) and the Swedish Research Council VR (621-2011-3492 / B0349201) are also acknowledged for financial support.

References

[1] P. Eklund, J. Emmerlich, H. Högberg, O. Wilhelmsson, P. Isberg, J. Birch, et al., Structural, electrical, and mechanical properties of nc-TiC/a-SiC nanocomposite thin films, J. Vac. Sci. Technol. B Microelectron. Nanom. Struct. 23 (2005) 2486, http://dx.doi.org/10.1116/1.2131081.
[2] P. Eklund, Novel ceramic nc-TiC/a-SiC nanocomposite coatings for electrical contact applications, Surf. Eng. 23 (2007) 406, http://dx.doi.org/10.1179/174329407X239126.
[3] E. Lewin, O. Wilhelmsson, U. Jansson, Nanocomposite nc-TiC/a-C thin films for electrical contact applications, J. Appl. Phys. 100 (2006) 54303–54310, http://dx.doi.org/10.1063/1.2336302.
[4] M. Andersson, J. Högström, S. Urbonaite, A. Furlan, L. Nyholm, U. Jansson, Deposition and characterization of magnetron sputtered amorphous Cr–C films, Vacuum 86 (2012) 1408–1416, http://dx.doi.org/10.1016/j.vacuum.2012.01.021.
[5] J. Högström, M. Andersson, U. Jansson, F. Björefors, L. Nyholm, On the evaluation of corrosion resistances of amorphous chromium–carbon thin-films, Electrochim. Acta 122 (2014) 224–233, http://dx.doi.org/10.1016/j.electacta.2013.11.130.
[6] K. Nygren, M. Andersson, J. Högström, W. Fredriksson, K. Edström, L. Nyholm, et al., Influence of deposition temperature and amorphous carbon on microstructure and oxidation resistance of magnetron sputtered nanocomposite CrC films, Appl. Surf. Sci. 305 (2014) 143–153, http://dx.doi.org/10.1016/j.apsusc.2014.03.014.
[7] C.P. Mulligan, D. Gall, CrN–Ag self-lubricating hard coatings, Surf. Coat. Technol. 200 (2005) 1495–1500, http://dx.doi.org/10.1016/j.surfcoat.2005.08.063.
[8] L. Incerti, A. Rota, S. Valeri, A. Miguel, J.A. García, R.J. Rodríguez, et al., Nanostructured self-lubricating CrN–Ag films deposited by PVD arc discharge and magnetron sputtering, Vacuum 85 (2011) 1108–1113, http://dx.doi.org/10.1016/j.vacuum.2011.01.022.
[9] P. Bílek, P. Jurči, M. Hudáková, M. Pašák, M. Kusý, J. Bohovičová, Cr2N–7Ag nanocomposite thin films deposited on Vanadis 6 tool steel, Appl. Surf. Sci. 307 (2014) 13–19, http://dx.doi.org/10.1016/j.apsusc.2014.03.044.
[10] P. Jurči, I. Dlouhý, Coating of Cr–V ledeburitic steel with CrN containing a small addition of Ag, Appl. Surf. Sci. 257 (2011) 10581–10589, http://dx.doi.org/10.1016/j.apsusc.2011.07.054.
[11] K. Kutschej, C. Mitterer, C.P. Mulligan, D. Gall, High-temperature tribological behavior of CrN–Ag self-lubricating coatings, Adv. Eng. Mater. 8 (2006) 1125–1129, http://dx.doi.org/10.1002/adem.200600131.
[12] C.P. Mulligan, T.A. Blanchet, D. Gall, CrN–Ag nanocomposite coatings: tribology at room temperature and during a temperature ramp, Surf. Coat. Technol. 204 (2010) 1388–1394, http://dx.doi.org/10.1016/j.surfcoat.2009.09.018.
[13] L. Incerti, A. Rota, A. Ballestrazzi, E. Gualtieri, S. Valeri, Ag surface diffusion and out-of-bulk segregation in CrN-Ag nano-composite coatings, J. Nanosci. Nanotechnol. 11 (2011) 9260–9266, http://dx.doi.org/10.1166/jnn.2011.4299.
[14] C.P. Mulligan, T.A. Blanchet, D. Gall, CrN–Ag nanocomposite coatings: high-temperature tribological response, Wear 269 (2010) 125–131, http://dx.doi.org/10.1016/j.wear.2010.03.015.
[15] S.M. Aouadi, D.P. Singh, D.S. Stone, K. Polychronopoulou, F. Nahif, C. Rebholz, et al., Adaptive VN/Ag nanocomposite coatings with lubricious behavior from 25 to 1000 °C, Acta Mater. 58 (2010) 5326–5331, http://dx.doi.org/10.1016/j.actamat.2010.06.006.
[16] W. Gulbiński, T. Suszko, Thin films of Mo2N/Ag nanocomposite—the structure, mechanical and tribological properties, Surf. Coat. Technol. 201 (2006) 1469–1476, http://dx.doi.org/10.1016/j.surfcoat.2006.02.017.
[17] C.C. Tseng, J.H. Hsieh, W. Wu, S.Y. Chang, C.L. Chang, Surface and mechanical characterization of TaN–Ag nanocomposite thin films, Thin Solid Films 516 (2008) 5424–5429, http://dx.doi.org/10.1016/j.tsf.2007.07.114.
[18] D.S. Stone, J. Migas, A. Martini, T. Smith, C. Muratore, A.A. Voevodin, et al., Adaptive NbN/Ag coatings for high temperature tribological applications, Surf. Coat. Technol. 206 (2012) 4316–4321, http://dx.doi.org/10.1016/j.surfcoat.2012.04.054.
[19] S. Calderon Velasco, V. Lopez, C.F. Almeida Alves, A. Cavaleiro, S. Carvalho, Structural and electrochemical characterization of Zr–C–N–Ag coatings deposited by DC dual magnetron sputtering, Corros. Sci. 80 (2014) 229–236, http://dx.doi.org/10.1016/j.corsci.2013.11.036.
[20] P. Basnyat, B. Luster, Z. Kertzman, S. Stadler, P. Kohli, S. Aouadi, et al., Mechanical and tribological properties of CrAlN–Ag self-lubricating films, Surf. Coat. Technol. 202 (2007) 1011–1016, http://dx.doi.org/10.1016/j.surfcoat.2007.05.088.
[21] J.L. Endrino, J.J. Nainaparampil, J.E. Krzanowski, Microstructure and vacuum tribology of TiC–Ag composite coatings deposited by magnetron sputtering-pulsed laser deposition, Surf. Coat. Technol. 157 (2002) 95–101, http://dx.doi.org/10.1016/S0257-8972(02)00138-X.
[22] J.L. Endrino, J.J. Nainaparampil, J.E. Krzanowski, Magnetron sputter deposition of WC–Ag and TiC–Ag coatings and their frictional properties in vacuum environments, Scr. Mater. 47 (2002) 613–618, http://dx.doi.org/10.1016/S1359-6462(02)00236-1.
[23] M. Magnuson, M. Andersson, J. Lu, L. Hultman, U. Jansson, Electronic structure and chemical bonding of amorphous chromium carbide thin films, J. Phys. Condens. Matter 24 (2012) 225004, http://dx.doi.org/10.1088/0953-8984/24/22/225004.
[24] M.P. Seah, Summary of ISO/TC 201 Standard: VII ISO 15472:2001 surface chemical analysis, x-ray photoelectron spectrometers. Calibration of energy scales, Surf. Interface Anal. 31 (2001) 721–723, http://dx.doi.org/10.1002/sia.1076.
[25] T. Holland, S. Redfern, Unit cell refinement from powder diffraction data: the use of regression diagnostics, Mineral. Mag. 61 (1997) 65–77.
[26] W.C. Oliver, G.M. Pharr, An improved technique for determining hardness and elastic-modulus using load and displacement sensing indentation experiments, J. Mater. Res. 7 (1992) 1564–1583, http://dx.doi.org/10.1557/JMR.1992.1564.
[27] K. Nygren, M. Samuelsson, A. Flink, H. Ljungcrantz, Å. Kassman Rudolphi, U. Jansson, Growth and characterization of chromium carbide films deposited by high rate reactive magnetron sputtering for electrical contact applications, Surf. Coat. Technol. 260 (2014) 326–334, http://dx.doi.org/10.1016/j.surfcoat.2014.06.069.
[28] J. Lauridsen, P. Eklund, J. Jensen, A. Furlan, A. Flink, A.M. Andersson, et al., Effects of A-elements (A = Si, Ge or Sn) on the structure and electrical contact properties of Ti–A–C–Ag nanocomposites, Thin Solid Films 520 (2012) 5128–5136, http://dx.doi.org/10.1016/j.tsf.2012.04.037.
[29] Standard test method for wear testing with a pin-on-disk apparatus, ASTM G99-05(2010), ASTM International, West Conshohocken, 2010http://dx.doi.org/10.1520/G0099-05R10.
[30] H.E. Swanson, E. Tatge, National bureau of standards (U.S.) Circular 539, vol. 1 1953, p. 23.
[31] National bureau of standards (U.S) monograph 25, 21 1985, p. 60.
[32] U. Wiklund, M. Nordin, O. Wänstrand, M. Larsson, Evaluation of a flexible physical vapor deposited TiC–C coating system, Surf. Coat. Technol. 124 (2000) 154, http://dx.doi.org/10.1016/S0257-8972(99)00627-1.
[33] O. Tengstrand, N. Nedfors, M. Andersson, J. Lu, U. Jansson, A. Flink, et al., Beam-induced crystallization of amorphous Me–Si–C (Me = Nb or Zr) thin films during transmission electron microscopy, MRS Commun. 3 (2013) 151–155, http://dx.doi.org/10.1557/mrc.2013.31.
[34] O. Tengstrand, N. Nedfors, M. Andersson, J. Lu, U. Jansson, A. Flink, et al., Model for electron-beam-induced crystallization of amorphous Me–Si–C (Me = Nb or Zr) thin films, J. Mater. Res. 29 (2014) 2854–2862, http://dx.doi.org/10.1557/jmr.2014.345.
[35] C.P. Mulligan, P.A. Papi, D. Gall, Ag transport in CrN–Ag nanocomposite coatings, Thin Solid Films 520 (2012) 6774–6779, http://dx.doi.org/10.1016/j.tsf.2012.06.082.
[36] G. Gassner, J. Patscheider, P.H. Mayrhofer, E. Hegedus, L. Toth, I. Kovacs, et al., Structure of sputtered nanocomposite CrCx/a-C:H thin films, J. Vac. Sci. Technol. B 24 (2006) 1837–1843, http://dx.doi.org/10.1116/1.2216713.
[37] K. Bewilogua, H.-J. Heinitz, B. Rau, S. Schulze, A chromium carbide phase with B1 structure in thin films prepared by ion plating, Thin Solid Films 167 (1988) 233–244, http://dx.doi.org/10.1016/0040-6090(88)90500-7.
[38] A. Abdulkadhim, M. to Baben, T. Takahashi, V. Schnabel, M. Hans, C. Polzer, et al., Crystallization kinetics of amorphous Cr2AlC thin films, Surf. Coat. Technol. 206 (2011) 599–603, http://dx.doi.org/10.1016/j.surfcoat.2011.06.003.
[39] T. Castro, R. Reifenberger, E. Choi, R. Andres, Size-dependent melting temperature of individual nanometer-sized metallic clusters, Phys. Rev. B 42 (1990) 8548–8556, http://dx.doi.org/10.1103/PhysRevB.42.8548.
[40] Y.-M. Chiang, D.I. Birnie, W.D. Kingery, Physical Ceramics; Principles for Ceramic Science and Engineering, John Wiley & Sons, Inc, 1997.